energies

Article

Development of a Thermal Energy Harvesting Converter with Multiple Inputs and an Isolated Output

Yeu-Torng Yau [1], Kuo-Ing Hwu [2,*] and Jenn-Jong Shieh [3]

[1] Department of Ph.D. Program, Prospective Technology of Electrical Engineering and Computer Science, National Chin-Yi University of Technology, No. 57, Sec. 2, Zhongshan Rd., Taiping Dist., Taichung 41170, Taiwan; pabloyau@ncut.edu.tw
[2] Department of Electrical Engineering, College of Electrical Engineering & Computer Science, National Taipei University of Technology, 1, Sec. 3, Zhongxiao E. Rd., Taipei 10608, Taiwan
[3] Department of Electrical Engineering, College of Information & Electrical Engineering, Feng Chia University, No. 100, Wenhwa Road, Seatwen, Taichung 40724, Taiwan; jjshieh@fcu.edu.tw
* Correspondence: eaglehwu@ntut.edu.tw; Tel.: +88-62-2771-2171 (ext. 2159)

Abstract: In this paper, an isolated multi-input single-output (MISO) converter is developed and applied to a thermoelectric energy conversion system to harvest thermal energy. The thermoelectric generators have individual maximum power point tracking functions. Furthermore, such a converter has a high step-up voltage conversion ratio. In addition, the presented converter is imposed on the thermoelectric energy conversion system with the three-point weighting strategy adopted to realize the maximum power point tracking (MPPT). In this paper, the basic principles of this converter are first described and analyzed, and finally some simulated and experimental results are offered to verify the feasibility and effectiveness of such a thermal energy harvesting system.

Keywords: coupled inductor; FPGA; galvanic isolation; MISOC; thermal energy harvesting; thermoelectric module; three-point perturbation and observation method

Citation: Yau, Y.-T.; Hwu, K.-I.; Shieh, J.-J. Development of a Thermal Energy Harvesting Converter with Multiple Inputs and an Isolated Output. *Energies* **2022**, *15*, 273. https://doi.org/10.3390/en15010273

Academic Editor: Andrea Frazzica

Received: 26 November 2021
Accepted: 20 December 2021
Published: 31 December 2021

1. Introduction

As generally recognized, from the point of view of industrial applications, 50% of generated electricity is used, while the remainder is wasted via heat. Accordingly, if the heat can be changed to electricity, then the energy conversion efficiency can be increased, and the pollution due to exhaust heat and emissions due to exhaust gas can be decreased [1]. At present, many methods have been proposed to recycle exhaust heat into electricity—for example, the organic Rankine cycle, combination of power and heat, thermoelectric generators (TEGs), etc.; of these, TEGs have many features, such as small size, no noise, easy maintenance, easy extension, etc. In fact, the process of recycling thermal energy is quite similar to that of recycling solar energy—both of which require the maximum power point tracking (MPPT) to harvest thermal energy efficiently.

Therefore, there are several configurations for converting heat to electricity using a TEG. TEG-based electrical systems can be divided into three types: single TEGs [2,3], distributed TEGs [2–4], and centralized TEGs [2]. The first type adopts a single heat source, while the other two types use multiple heat sources. However, the first type has a limited power level, the second type is limited in terms of size and cost, and the third faces the problem of the failure of one TEG.

Therefore, a multiple-input TEG system is proposed to conquer these disadvantages. To construct a single-stage thermoelectric energy conversion system with multiple TEG inputs, a high step-up converter is indispensable. The authors of [5–14] propose several kinds of multi-input single-output converters (MISOCs) with non-isolation. The authors of [6] utilized a switched-capacitor circuit so that a high voltage gain could be achieved.

The authors of [5,11,14] adopted elementary circuit configurations, leading to the corresponding voltage gains not being high. The authors of [11] employed an elementary circuit configuration together with an auxiliary circuit, such that the zero-voltage switching (ZVS) could be achieved but the accompanying voltage gain was not high. The authors of [6,9,10] utilized coupled inductors so that the voltage gains could be improved and the ZVS could be realized. However, if the number of input voltages is increased, then the number of coupled inductors and switches is increased, resulting in the huge size needed. The circuit concept displayed in [12] is derived from [14], and this converter adopts only a single inductor to obtain a result identical to that of [14], thus decreasing the size significantly; however, this converter employs an elementary circuit configuration, resulting in the voltage gain not being high; moreover, the control of such a converter is relatively complicated. The authors of [13,15] achieved high step-up voltage gains by utilizing bootstrap circuits; however, these circuits have automatic current balance, making them unsuitable for MPPT use. Consequently, the authors of [16] presented interleaved switches for the circuit shown in [15] to conquer this problem, so that each thermoelectric generator would have its own MPPT function.

For galvanic isolation to be considered, the authors of [17,18] proposed an isolated MISO high-step-up converter; however—considering that the higher the turns ratio, the greater the leakage inductance and the larger the primary-side current—the actual voltage conversion ratio remains not particularly high. In [19], the multiple inputs had individual resonant networks and coupled inductors, causing switches to have ZVS turn-on, the number of components to be relatively large, and the corresponding maximum voltage gain to be less than 1.5. In [20], a single coupled inductor was used to harvest energy from multiple heat sources; however, the duty cycle for each input has its own limitations, and the overall voltage gain is determined only by the turns ratio.

In fact, none of the converters described previously—except for the converter displayed in [16]—are used in thermoelectric systems. Accordingly, an isolated MISOC circuit is proposed herein and imposed on a thermoelectric energy conversion system.

2. Features of the Thermoelectric Module

The operation of the thermoelectric module is based on the Seebeck effect; this means that the movement of major P-type and N-type carriers due to temperature differences between the hot side and the cold side forms a current. In Figure 1a, the model of the thermoelectric module is represented by one open-circuit voltage V_{oc} and one internal resistance R_{teg}. In this figure, the voltage across the variable load resistance R_L is V_{teg}, and the current flowing into R_L is I_{teg}. In Figure 1b, if R_L is infinite, then V_{teg} is equal to V_{oc}; if R_L is zero, then I_{teg} is equal to I_{sc} (In Figure 1c), which is V_{oc} divided by R_{teg}. Therefore, based on the maximum power transfer theory under the condition that $R_L = R_{teg}$ [21,22], we can find the maximum power point (MPP) at:

$$V_{teg} = 0.5V_{oc} \text{ and } I_{teg} = 0.5I_{sc} \quad (1)$$

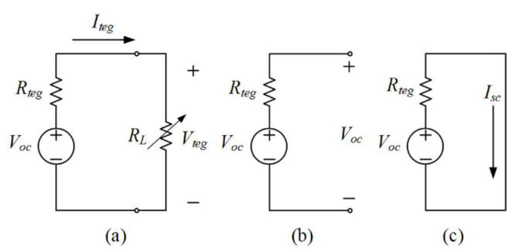

Figure 1. Deduction of the TEG MPP.

Hence, the maximum power—represented as P_{mpp}—is identical to:

$$P_{mpp} = 0.25V_{oc} \cdot I_{sc} \tag{2}$$

Accordingly, the P–I–V curves of TEG are drawn in Figure 2. From this figure, it can be seen that these curves are of high symmetricity.

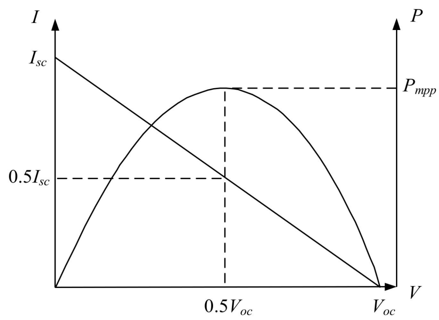

Figure 2. TEG P–I–V Curves.

3. Three-Point Weighting Strategy for MPPT

Based on Figure 1, the three-point weighting strategy was adopted to derive the maximum power transfer from the TEG to the output. Figure 3 displays the operating procedure of this method, and the corresponding operation is shown in Figure 4 with three cases: for case 1, $P_a > P_b > P_c$; for case 2, $P_a < P_b < P_c$; for case 3, $P_b > P_a$ and P_c. As in case 3, the point of the maximum power can be obtained. Note that D_{mpp}, D_a, D_b, and D_c are defined to be the duty cycles at the maximum power point, point a, point b, and point c, respectively.

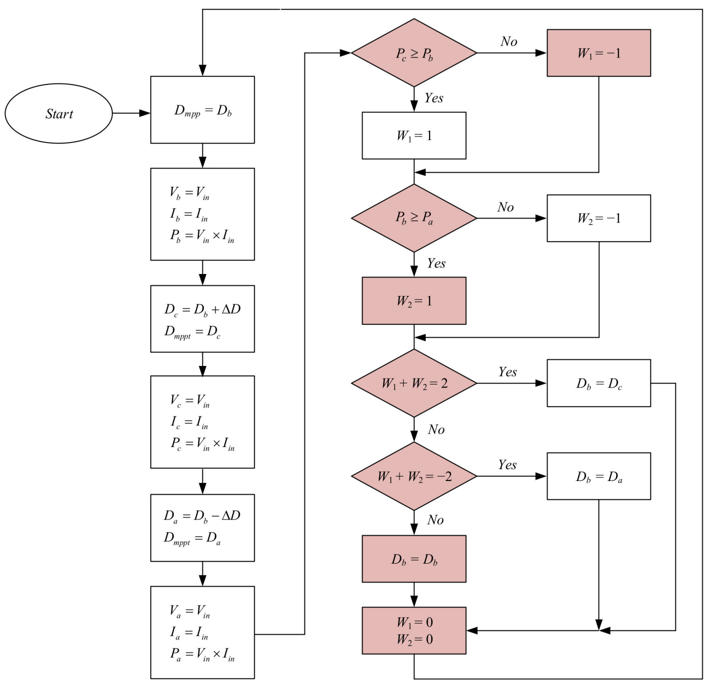

Figure 3. Operating procedure of the three-point weighting strategy for MPPT.

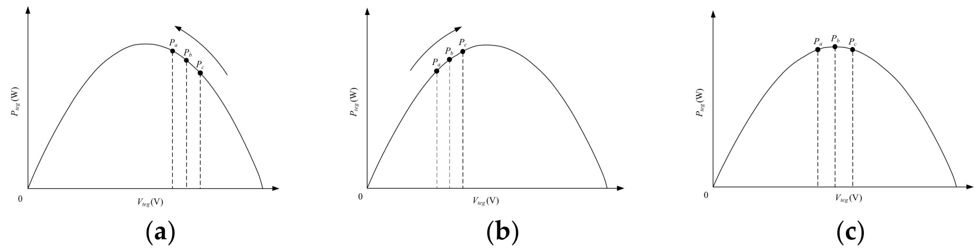

Figure 4. Three cases for the three-point weighting strategy. (**a**), $P_a > P_b > P_c$; (**b**), $P_a < P_b < P_c$; (**c**), $P_b > P_a$ and P_c.

4. Proposed Isolated MISOC

Figure 5 shows the proposed two-input single-output isolated high-step-up converter, which is composed of one input inductor L, one output inductor L_o, one coupled inductor constructed by one inductance, one leakage inductance with the primary winding N_p, the secondary winding N_s, a turns ratio of ($n = N_p/N_s$), two main switches S_1 and S_2, three charge pump capacitors C_1, C_2, and C_3, three diodes D_1, D_2, and D_3, and one output capacitor C_o. As for the output load, it consists of one output resistor R_o.

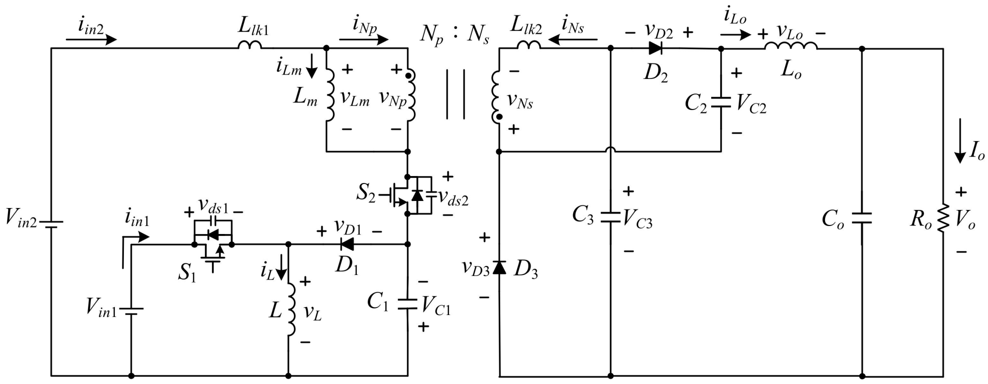

Figure 5. Proposed isolated MISOC circuit.

Before dealing with this section, we must first define some symbols shown in Figure 5 and several constraints, as follows: (1) the two input voltages are signified by V_{in1} and V_{in2}; (2) the two input currents are indicated by i_{in1} and i_{in2}; (3) the output current is expressed by I_o; (4) the output voltage is denoted by V_o; (5) the voltages across C_1, C_2, and C_3 are represented by V_{C1}, V_{C2}, and V_{C3}, respectively; (6) the pulse-width modulation (PWM) signals for S_1 and S_2 are signified by v_{gs1} and v_{gs2}, respectively; (7) the voltages across L, L_m, L_o, N_p, N_s, and L_{lk} are indicated by v_L, v_{Lm}, v_{Lo}, v_{Np}, v_{Ns}, and v_{lk}, respectively; (8) the voltages across D_1, D_2, and D_3 are described by v_{D1}, v_{D2}, and v_{D3}, respectively; (9) the currents in L, L_m, L_o, N_p, and N_s are signified by i_L, i_{Lm}, i_{Lo}, i_{Np}, and i_{Ns}, respectively; (10) the currents in D_1, D_2, and D_3 are denoted by i_{D1}, i_{D2}, and i_{D3}, respectively; (11) the duty cycles of v_{gs1} and v_{gs2} are expressed by D_a and D_b, respectively, under the same switching period of T_s; (12) all the components are regarded as ideal, except for S_1 and S_2; (13) the converter works in the continuous current mode (CCM); (14) all of the waveforms are drawn in the steady state, and four states over one cycle are illustrated in Figure 6, to be analyzed as follows:

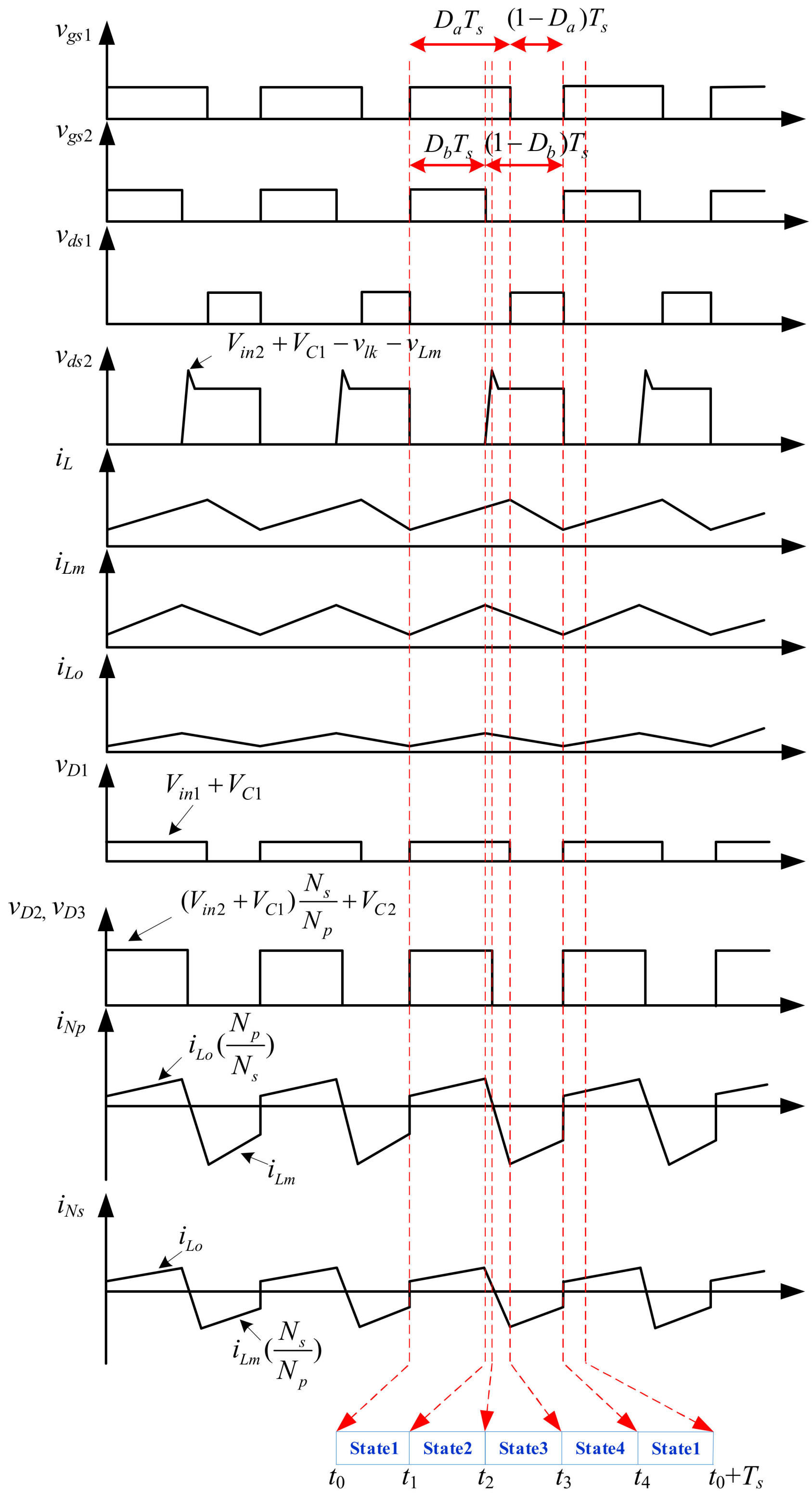

Figure 6. Illustrated waveforms relevant to the proposed isolated MISOC circuit.

4.1. Operational Behavior

State 1 [$t_o \leq t \leq t_1$]: As illustrated in Figure 7, S_1 and S_2 are turned on, whereas D_1, D_2, and D_3 are reverse-biased. During this time interval, L is magnetized by V_{in1}, whereas L_m, L_{lk}, and L_o are magnetized by V_{in2} and C_1. At the same time, C_2 and C_3 are series-connected, and release energy to the load. In addition, D_1 is reverse-biased with the voltage of $V_{in1} + V_{C1}$, D_2 is reverse-biased with the voltage of $(V_{in2} + V_{C1})/n + V_{C2}$, and D_3 is reverse-biased with the voltage of $(V_{in2} + V_{C1})/n + V_{C3}$ with $V_{C2} = V_{C3}$.

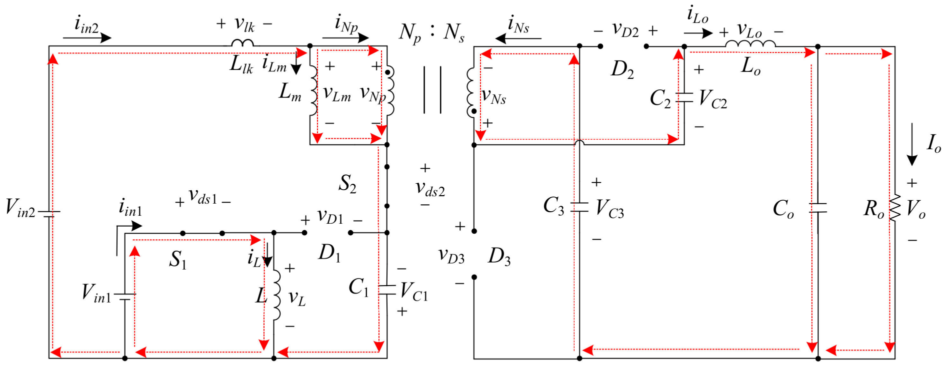

Figure 7. State 1 power flow.

State 2 [$t_1 \leq t \leq t_2$]: As illustrated in Figure 8, S_1 remains in the on-state, but S_2 is turned off, whereas D_1, D_2, and D_3 remain reverse-biased. During this time interval, L is still magnetized by V_{in1}, whereas L_m, L_{lk}, and L_o are demagnetized. Since i_{Np} remains in the positive direction, the second-side circuit operation is the same as in state 1. In addition, the leakage inductance i_{lk} releases energy as well as charging the parasitic capacitor of S_2, leading to a spike voltage on S_2. The moment i_{N2} falls to zero, this state proceeds to the end.

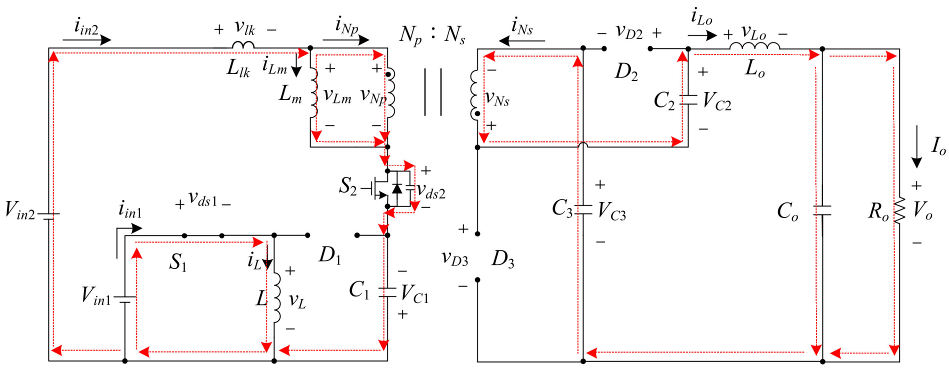

Figure 8. State 2 power flow.

State 3 [$t_2 \leq t \leq t_3$]: As illustrated in Figure 9, S_1 remains in the on-state, but S_2 remains in the off-state, whereas D_1 is turned off but D_2 and D_3 remain in the on-state. During this time interval, L is still magnetized by V_{in1}, whereas L_m and L_o are still demagnetized, and charge C_2 and C_3, thereby causing C_2 and C_3 to be paralleled with V_{C2} = V_{C3}. Once the switch S_1 is turned off, this state ends.

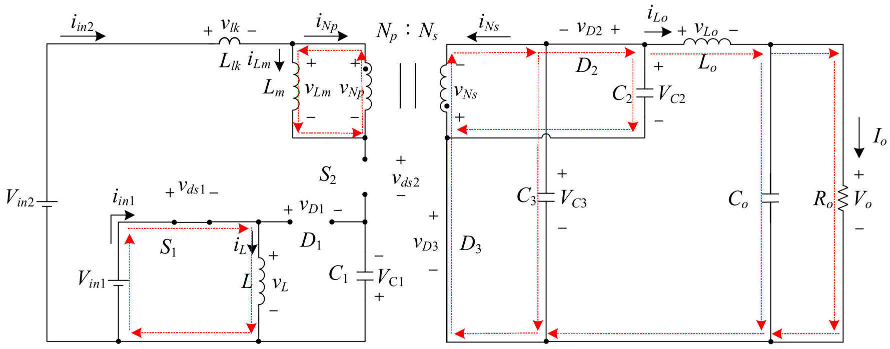

Figure 9. State 3 power flow.

State 4 [$t_3 \leq t \leq t_4$]: As illustrated in Figure 10, S_1 and S_2 are both off, whereas D_1, D_2, and D_3 are all reverse-biased. During this time interval, L releases energy to C_1. In the meantime, L_m is still demagnetized, so the secondary-side circuit operation is the same as in state 3. As soon as S_1 and S_2 are turned on, this state comes to an end, and the next period starts.

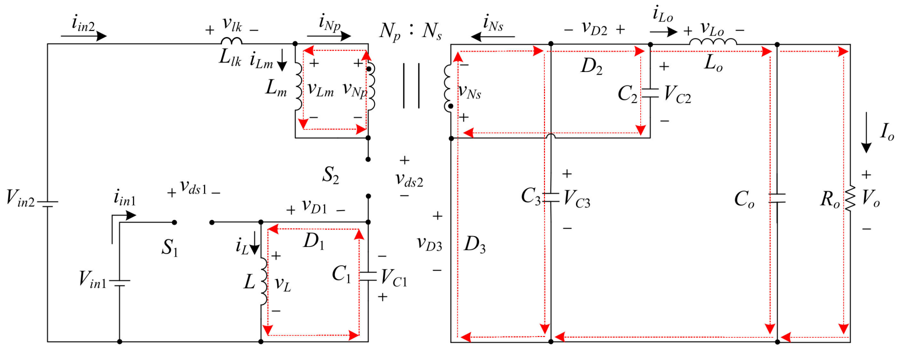

Figure 10. State 4 power flow.

4.2. Output Voltage

To conveniently obtain the voltages on C_1, C_2, C_3, and C_o, only states 1, 3, and 4 are taken into account, and L_{lk} is omitted. First, the turns ratio of the transformer is defined as follows:

$$\frac{N_p}{N_s} < 1 \text{ and } n < 1 \tag{3}$$

As illustrated in state 1 in Figure 7, based on Kirchhoff's voltage law, the respective voltages across the input inductor L, the magnetizing inductance L_m, and the output inductor L_o are:

$$v_L = V_{in1} \tag{4}$$

$$v_{Lm} = V_{in2} + V_{C1} \tag{5}$$

$$v_{Lo} = \frac{1}{n}(V_{in2} + V_{C1}) + V_{C2} + V_{C3} - V_o \tag{6}$$

As illustrated in state 3 in Figure 9, based on Kirchhoff's voltage law, the respective voltages across the input inductor L, the magnetizing inductance L_m, and the output inductor L_o are:

$$v_L = V_{in1} \tag{7}$$

$$v_{Lm} = -nV_{C2} = -nV_{C3} \tag{8}$$

$$v_{Lo} = V_{C2} - V_o = V_{C3} - V_o \tag{9}$$

As illustrated in state 4 in Figure 10, based on Kirchhoff's voltage law, the respective voltages across the inductor L, the magnetizing inductance L_m, and the output inductor L_o are:

$$v_L = -V_{C1} \tag{10}$$

$$v_{Lm} = -nV_{C2} = -nV_{C3} \tag{11}$$

$$v_{Lo} = V_{C2} - V_o = V_{C3} - V_o \tag{12}$$

In the steady state, the input inductor L, the magnetizing inductance L_m, and the output inductor L_o should obey the volt–second balance, so the respective associated equations can be attained based on (4) and (10), (5) and (8), and (6) and (9):

$$V_{in1}D_aT_s + (-V_{C1})(1-D_a)T_s = 0 \tag{13}$$

$$(V_{in2} + V_{C1})D_bT_s + (-nV_{C2})(1-D_b)T_s = 0 \tag{14}$$

$$\begin{aligned}&[\tfrac{1}{n}(V_{in2} + V_{C1}) + V_{C2} + V_{C3} - V_o]D_bT_s \\ &+(V_{C2} - V_o)(1-D_b)T_s = 0\end{aligned} \tag{15}$$

Rearranging (13), (14), and (15), respectively, yields:

$$\frac{V_{C1}}{V_{in1}} = \frac{D_a}{1-D_a} \tag{16}$$

$$V_{C2} = V_{C3} = \frac{1}{n}(V_{in2} + V_{C1})\left(\frac{D_b}{1-D_b}\right) \tag{17}$$

$$V_o = \frac{2}{n}[V_{in2} + V_{C1}]\left(\frac{D_b}{1-D_b}\right) \tag{18}$$

By substituting (16) into (17) and (18), the voltages V_{C2} and V_{C3} can be attained as follows:

$$V_{C2} = V_{C3} = \frac{1}{n}\left[V_{in2} + V_{in1}\left(\frac{D_a}{1-D_a}\right)\right]\left(\frac{D_b}{1-D_b}\right) \tag{19}$$

Therefore, the voltage V_o can be represented as:

$$V_o = V_{C2} + V_{C3} = \frac{2}{n}\left[V_{in2} + V_{in1}\left(\frac{D_a}{1-D_a}\right)\right]\left(\frac{D_b}{1-D_b}\right) \tag{20}$$

4.3. Boundary Condition for L

For convenience of analysis, it is assumed that the input power and the output power are identical, the input power is separated, and the input currents for the two thermoelectric generators are the same, namely, $I_{in1} = I_{in2} = I_{in}$.

As there is no power loss in this operating converter, the following equation can be obtained:

$$P_o = P_{in1} + P_{in2} = P_{o1} + P_{o2} \tag{21}$$

where P_o is the output power, and P_{in1} and P_{in2} are the two input powers of the two inputs, whereas P_{o1} and P_{o2} are the corresponding output powers of the two inputs.

From (21), the formula of the first output power is:

$$\begin{aligned}&P_{o1} = P_{in1} \\ &\Rightarrow V_{C1} \times I_{C1} = V_{in1} \times I_{in}\end{aligned} \tag{22}$$

where I_{C1} is the DC current in C_1.

For convenience of analysis, by assuming that the load resistance of the first input is R_1, the current flowing through R_1 can be represented as follows:

$$I_{C1} = \frac{V_{C1}}{R_1} \tag{23}$$

Therefore, substituting (16) and (23) into (22) yields:

$$\frac{{V_{C1}}^2}{R_1} = V_{in1} \times I_{in} = \frac{{D_a}^2 \times {V_{in1}}^2}{(1 - D_a)^2 \times R_1} \tag{24}$$

Since the ripple current in L—represented as Δi_L—can be indicated by:

$$\Delta i_L = \frac{v_L \times \Delta t}{L} \tag{25}$$

Substituting (4) into (25) yields:

$$\Delta i_L = \frac{V_{in1}}{L} D_a T_s \tag{26}$$

Hence, as $2I_L > \Delta i_L$, L will work in CCM; that is:

$$\begin{aligned} &2I_L \geq \Delta i_L \\ &\Rightarrow 2 \times \tfrac{D_a \times V_{in1}}{(1-D_a)^2 \times R_1} \geq \tfrac{V_{in1}}{L} D_a T_s \\ &\Rightarrow \tfrac{2L}{R_1 T_s} \geq (1 - D_a)^2 \\ &\Rightarrow K_L \geq K_{crit\_L}(D_a) \end{aligned} \tag{27}$$

where $K_L = \frac{2L}{R_1 T_s}$ and $K_{crit\_L}(D_a) = (1 - D_a)^2$.

From (27), it can be seen that if $K_L \geq K_{crit\_L}(D_a)$ holds, L works in CCM; if not, L will work in the discontinuous current mode (DCM). Hence, the boundary curve between two modes can be plotted as shown in Figure 11.

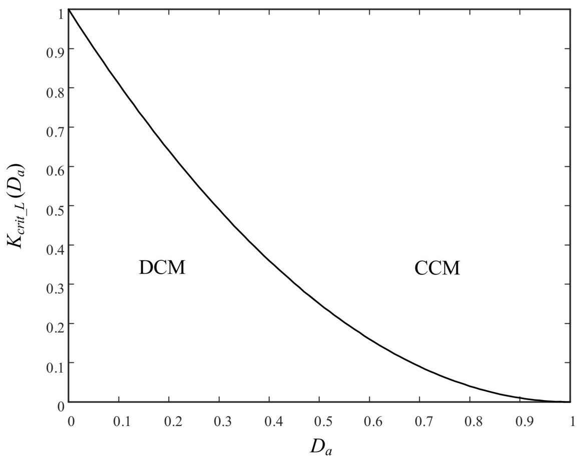

Figure 11. Boundary curve between CCM and DCM for L.

4.4. Boundary Curve of L_m

For convenience of analysis, it is assumed that the input power P_{in} is identical to the output power P_o, that the input power is separated, and that the input currents for the two thermoelectric generators are the same, namely, $I_{in1} = I_{in2} = I_{in}$. At the same time, from Figure 5, it can be seen that the average current is zero for the charge pump capacitors C_2 and C_3. Therefore, the average current in the secondary-side winding, I_{Ns}, is identical to the average current in the output inductor, I_{Lo}. Figure 12 shows the equivalent model for the DC current analysis of the coupled inductor.

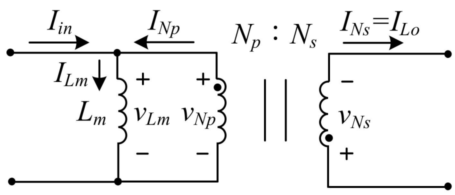

Figure 12. Equivalent model for DC current analysis of the coupled inductor.

According to state 2 and (5), the primary-side voltage v_{Np} can be expressed as follows:

$$v_{Np} = v_{Lm} = V_{in2} + V_{C1} \tag{28}$$

Since there is no power loss in the circuit, the resulting equation can be attained as:

$$P_{in} = P_o = V_o \times I_o \tag{29}$$

Rearranging (29) yields:

$$V_o \times I_o = (V_{in2} + V_{C1}) \times I_{in} \tag{30}$$

where:

$$I_o = \frac{V_o}{R_o} \tag{31}$$

From Figure 12, the average current of i_{Lm} can be represented by:

$$I_{Lm} = I_{Np} + I_{in} \tag{32}$$

and:

$$I_{Np} = \frac{I_{Ns}}{n} = \frac{I_o}{n} \tag{33}$$

Rearranging (30) yields:

$$I_{in} = \frac{V_o}{V_{in2} + V_{C1}} \times I_o \tag{34}$$

Substituting (18) and (28) into (34) yields:

$$I_{in} = \frac{2}{n} \times (\frac{D_b}{1 - D_b}) \times I_o \tag{35}$$

Substituting (33) and (35) into (32) yields:

$$I_{Lm} = \frac{I_o}{n}\left(\frac{1 + D_b}{1 - D_b}\right) \tag{36}$$

Substituting (31) into (36) yields:

$$I_{Lm} = \frac{V_o}{nR_o}\left(\frac{1 + D_b}{1 - D_b}\right) \tag{37}$$

In addition, the ripple current of i_{Lm}, $\Delta\, i_{Lm}$, can be obtained as follows:

$$\Delta i_{Lm} = \frac{v_{Lm} \times \Delta t}{L_m} \tag{38}$$

Substituting (28) into (38) yields:

$$\Delta i_{Lm} = \frac{V_{in2} + V_{C1}}{L_m} D_b T_s \tag{39}$$

Therefore, as $2I_{Lm} \geq \Delta i_{Lm}$, the magnetizing inductance L_m will operate in CCM; that is:

$$\begin{aligned}
&2I_{Lm} \geq \Delta i_{Lm} \\
&\Rightarrow 2 \times \tfrac{2V_o}{nR_o}\left(\tfrac{1+D_b}{1-D_b}\right) \geq \tfrac{V_{in2}+V_{C1}}{L_m} D_b T_s \\
&\Rightarrow \tfrac{2L_m}{R_o T_s} \geq n \times \tfrac{V_{in2}+V_{C1}}{V_o} \times \tfrac{D_b}{\left(\frac{1+D_b}{1-D_b}\right)} \\
&\Rightarrow \tfrac{2L_m}{R_o T_s} \geq n \times \tfrac{n(1-D_b)}{2D_b} \times \tfrac{D_b}{\left(\frac{1+D_b}{1-D_b}\right)} \\
&\Rightarrow \tfrac{2L_m}{R_o T_s} \geq \tfrac{[n(1-D_b)]^2}{2(1+D_b)} \\
&\Rightarrow K_{Lm} \geq K_{crit_Lm}(D_b)
\end{aligned} \tag{40}$$

where $K_{Lm} = \frac{2L_m}{R_o T_s}$ and $K_{crit\_Lm}(D_b) = \frac{[n(1-D_b)]^2}{2(1+D_b)}$.

From (40), under the turns ratio n = 0.5, if $K_{Lm} \geq K_{crit\_Lm}(D_b)$ holds, the inductance L_m will operate in CCM; if not, L_m will work in DCM. Accordingly, the boundary curve between CCM and DCM can be drawn as shown in Figure 13.

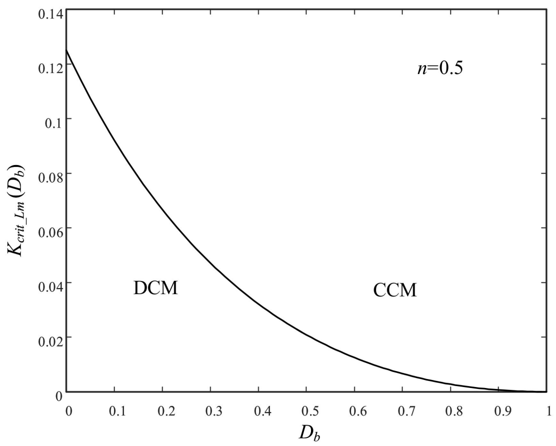

Figure 13. Boundary curve between CCM and DCM for L_m.

4.5. Boundary Condition for L_o

The average current of the output inductor I_{Lo} is identical to the output current I_o, namely:

$$I_{Lo} = I_o \tag{41}$$

Additionally:

$$I_o = \frac{V_o}{R_o} \tag{42}$$

According to (41), and by substituting (20) into (42), the following equation can be expressed:

$$I_{Lo} = \frac{\frac{2}{n}\left[V_{in2} + V_{in1}\left(\frac{D_a}{1-D_a}\right)\right]\left(\frac{D_b}{1-D_b}\right)}{R_o} \tag{43}$$

Moreover, the ripple current of i_{Lo}, represented as Δi_{Lo}, can be obtained as follows:

$$\Delta i_{Lo} = \frac{v_{Lo} \times \Delta t}{L_o} \tag{44}$$

Substituting (4) into (44) yields:

$$\Delta i_{Lo} = \frac{\frac{1}{n}(V_{in2} + V_{C1}) + V_{C2} + V_{C3} - V_o}{L_o} D_b T_s \tag{45}$$

Substituting (16) and (20) into (45) yields:

$$\Delta i_{Lo} = \frac{\frac{1}{n}\left[V_{in2} + \left(\frac{D_a}{1-D_a}\right)V_{in1}\right]}{L_o} D_b T_s \tag{46}$$

Substituting (4) into (25) yields:

$$\Delta i_L = \frac{V_{in1}}{L} D_a T_s \tag{47}$$

Therefore, as $2I_{Lo} \geq \Delta i_{Lo}$, the output inductor L_o operates in CCM; that is:

$$\begin{aligned} & 2 \times \frac{\frac{2}{n}\left[V_{in2}+V_{in1}\left(\frac{D_a}{1-D_a}\right)\right]\left(\frac{D_b}{1-D_b}\right)}{R_o} \\ & \geq \frac{\frac{1}{n}\left[V_{in2}+\left(\frac{D_a}{1-D_a}\right)V_{in1}\right]}{L_o} D_b T_s \\ & \Rightarrow \frac{2L_o}{R_o T_s} \geq \frac{(1-D_b)}{2} \\ & \Rightarrow K_{Lo} \geq K_{crit\_Lo}(D_b) \end{aligned} \tag{48}$$

where $K_{Lo} = \frac{2L_o}{R_o T_s}$ and $K_{crit\_Lo}(D_b) = \frac{(1-D_b)}{2}$.

From (48), it can be known that if $K_{Lo} \geq K_{crit\_Lo}(D_b)$ holds, the output inductor L_o works in CCM; if not, L_o operates in DCM. Therefore, the boundary curve between CCM and DCM can be sketched as shown in Figure 14.

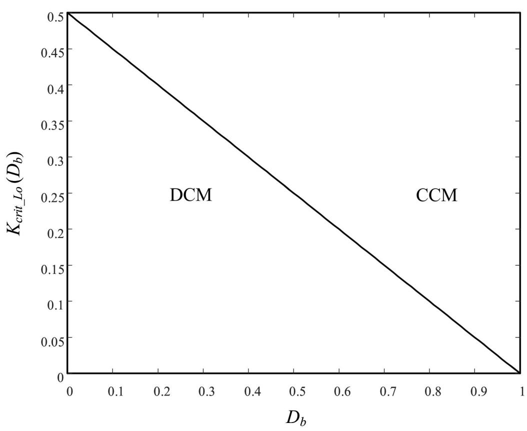

Figure 14. Boundary curve between CCM and DCM for L_o.

4.6. Topology Extension

As displayed in Figure 15, the proposed converter can be expanded to N inputs, where N is a positive integer; hence, its input count will be increased such that the thermal energy from all of the sources can be recycled.

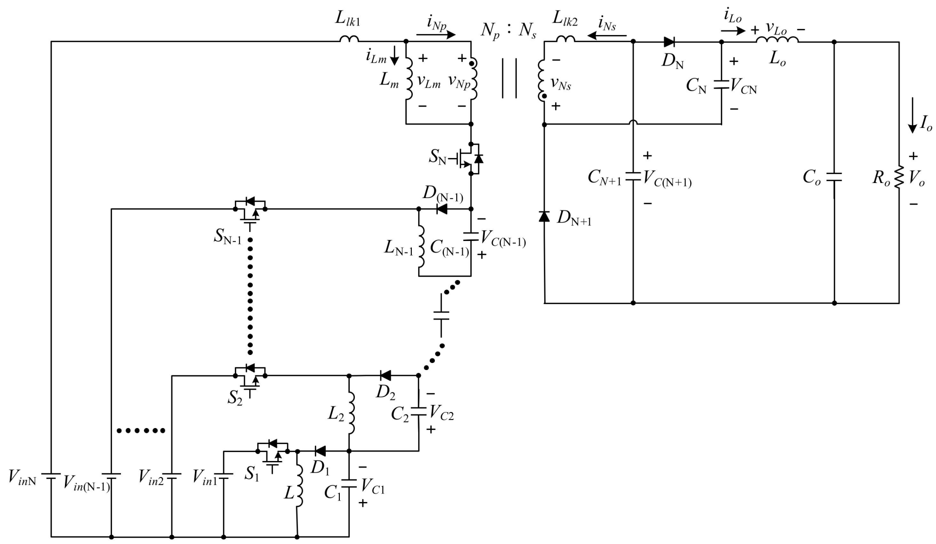

Figure 15. Expanded circuit.

5. Design Considerations

5.1. Thermoelectric Module Specifications

The thermoelectric modules adopted herein are called TGM-199-1.4-0.8, made by Kryotherm Co. There are two inputs in the proposed converter: the first input is fed by four series-connected thermoelectric modules, while the second input is fed by two series-connected thermoelectric modules. The associated specifications are displayed in Tables 1 and 2.

Table 1. Specifications for the first thermoelectric module.

Part Name	TGM-199-1.4-0.8
Size	40 × 40 × 3.2 mm
Number	Four in series
Maximum Power (P_{mpp1})	23.2 W
Voltage at MPP (V_{mpp1})	14 V
Current at MPP (I_{mpp1})	1.653 A
Open Voltage (V_{oc1})	27.6 V
Short Current (I_{sc1})	3.25 A
Cold-Side Temperature	80 °C
Hot-Side Temperature	180 °C

Table 2. Specifications for the second thermoelectric module.

Part Name	TGM-199-1.4-0.8
Size	40 × 40 × 3.2 mm
Number	Two in series
Maximum Power (P_{mpp2})	11.68 W
Voltage at MPP (V_{mpp2})	7.5 V
Current at MPP (I_{mpp2})	1.56 A
Open Voltage (V_{oc2})	13.95 V
Short Current (I_{sc2})	3.246 A
Cold-Side Temperature	80 °C
Hot-Side Temperature	180 °C

5.2. System Configuration Together with Design Concept and Experimental Strategy

Figure 16 shows the proposed isolated MISOC converter along with two thermoelectric generators, with an FPGA control kernel. According to Tables 1 and 2, the first TEG under MPPT has an output voltage of 14 V, and its output current is 1.653 A, whereas the second TEG under the MPPT has an output voltage of 7.5 V and an output current of 1.56 A. Therefore, the sum of the power generated from the two TEGs is 34.88 W. Accordingly, based on the above-mentioned factors, and by prescribing the output voltage of the converter at 100 V, Tables 3 and 4 display the system specifications and the respective converter specifications. An efficiency curve can be attained under the output voltage regulated at 100 V. Afterwards, the MPPT algorithm is imposed on this converter to harvest thermal energy; hence, some waveforms are measured. Moreover, under the control of MPPT, the needed digital signals—containing the input voltages and currents—are created after the analog-to-digital converters (ADCs), the field-programmable gate array (FPGA) shown in Table 5 is utilized to control such a system, and the gate-driving signals generated by the FPGA are passed to the switches. Note that since this circuit focuses on harvesting thermal energy, the output voltage sensor and the corresponding voltage mode controller are not displayed in Figure 16.

Table 3. System specifications.

Operating Mode	CCM
First Input Voltage (V_{in1})	7.5 V
Second Input Voltage (V_{in2})	14 V
Rated Output Voltage (V_o)	100 V
Rated Output Current ($I_{o,rated}$)/Power ($P_{o,rated}$)	348.8 mA/34.88 W
Minimum Output Current ($I_{o,min}$)/Power ($P_{o,min}$)	34.88 mA/3.488 W
Switching Frequency (f_s)/Power (T_s)	100 kHz/10 µs
$n = N_p/N_s$	0.5

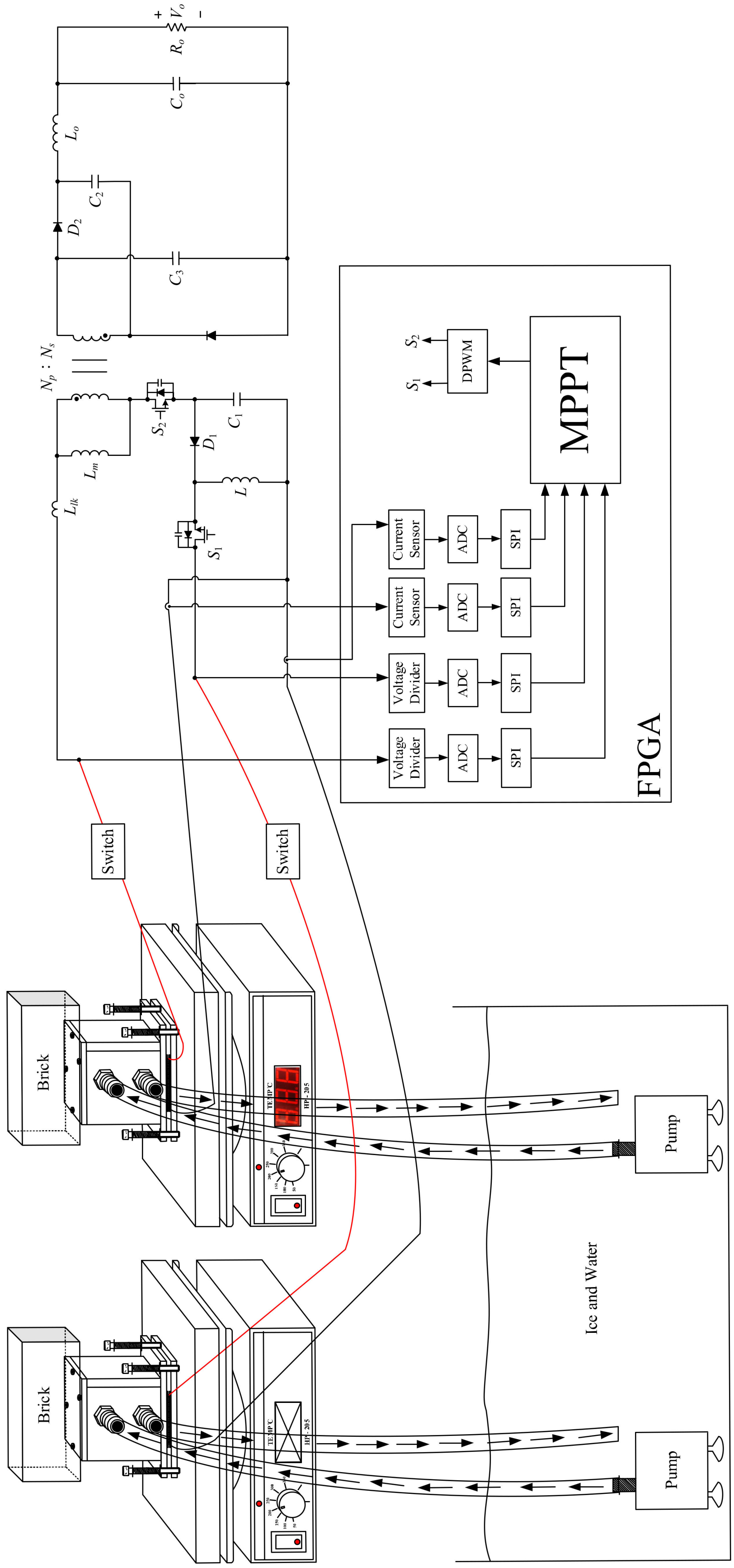

Figure 16. Thermoelectric system with the proposed isolated MISOC.

Table 4. Component specifications used in the isolated MISOC.

Components	Specifications
MOSFET Switch S_1	IRF3205 Z
MOSFET Switch S_2	STB120NF10T4
Diode D_1	STPS30L30CT
Diodes D_2, D_3	STPS20H100CT
Charge Pump Capacitor C_1	150 µF Electrolytic Capacitor
Charge Pump Capacitors C_2, C_3	47 µF Electrolytic Capacitor
Output Capacitor C_o	68 µF Electrolytic Capacitor
Input Inductor L	100 µH
Output Inductor L_o	4.32 mH
Coupled Inductor	L_m = 330 µH, n = 0.5
Isolated Gate Driver	FOD3182

Table 5. EP3C5E144C8N specifications.

Device	Logic Elements	Total RAM Bits	18 × 18 Multipliers	PLLs	User I/O Pins
EP3C5E144C8N	5136	423936	23	2	94

5.3. Calculation of Duty Cycles

Based on (39), with D_a equal to 0.6, the value of D_b will be calculated to be 0.4975.

$$\begin{aligned} & V_o = \tfrac{2}{n}\left[V_{in2} + V_{in1}\left(\tfrac{D_a}{1-D_a}\right)\right]\left(\tfrac{D_b}{1-D_b}\right) \\ & \Rightarrow 100 = \tfrac{2}{0.5}\left[14 + 7.5\left(\tfrac{0.6}{1-0.6}\right)\right]\left(\tfrac{D_b}{1-D_b}\right) \Rightarrow D_b = 0.4975 \end{aligned} \tag{49}$$

5.4. Design of L

By assuming that the inductor L works in CCM above 0.1 I_{mmp1}, and according to the following equation, the value of L_{min} can be derived as follows:

$$L_{min} = \frac{v_L \times D_a \times T_s}{2 \times 0.1 I_{mpp1} \div D_a} = \frac{7.5 \times 0.6^2 \times 10\ \mu}{2 \times 0.1 \times 1.56} = 86.54\ \mu\text{H} \tag{50}$$

Eventually, the value of L is set at 100 µH.

5.5. Design of L_o

By assuming that the inductor L_o works in CCM above $I_{o,min}$, and according to the following equations, the value of $L_{o,min}$ can be derived as follows:

$$v_{Lo} = \frac{1}{n}\left[V_{in2} + \left(\frac{D_a}{1-D_a}\right)V_{in1}\right] = \frac{1}{0.5}\left[14 + \left(\frac{0.6}{1-0.6}\right) \times 7.5\right] = 50.5\ \text{V} \tag{51}$$

$$L_{o,min} = \frac{v_{Lo} \times D_b \times T_s}{2 \times I_{o,\text{min}}} = \frac{50.5 \times 0.4975 \times 10\ \mu}{2 \times 34.88\ \text{m}} = 3.6\ \text{mH} \tag{52}$$

Eventually, the value of L_o is set at 4.32 mH.

5.6. Design of L_m

By assuming that the inductor L_m operates in CCM above $I_{o,min}$, and according to (40), the value of $L_{m,min}$ can be derived as follows:

$$\begin{aligned} L_{m,min} &= \tfrac{[n(1-D_b)]^2}{4(1+D_b)} \times T_s \times \tfrac{V_o}{I_{o,min}} \\ &= \tfrac{[0.5(1-0.4975)]^2}{4(1+0.4975)} \times 10\mu \times \tfrac{100}{34.88\text{m}} = 302\ \mu\text{H} \end{aligned} \tag{53}$$

Eventually, the value of L_m is set at 330 μH.

5.7. Design of C_1

By assuming that the maximum ripple voltage of C_1 is 1% of V_{C1}, and based on the following equations, the value of $C_{1,min}$ can be worked out as follows:

$$V_{C1} = \frac{D_a}{1-D_a} \times V_{in1} = \frac{0.6}{1-0.6} \times 7.5 = 11.25\ \text{V} \tag{54}$$

$$C_{1,min} = \frac{I_{in}}{D_a} \times \frac{(1-D_a)T_s}{0.01 \times V_{C1}} = \frac{1.56}{0.6} \times \frac{(1-0.6)10\mu}{0.01 \times 11.25} = 92\ \mu\text{F} \tag{55}$$

Eventually, the value of C_1 is set at 150 μF.

5.8. Design of C_2 and C_3

By assuming that the maximum ripple voltage of C_2 or C_3 is 0.1% of V_{C2} or V_{C3}, respectively, and based on (17), the value of $C_{2,min}$ or $C_{3,min}$ can be worked out as follows:

$$V_{C2} = V_{C3} = \frac{1}{n}(V_{in2} + V_{C1})\left(\frac{D_b}{1-D_b}\right) = \frac{1}{0.5}(14 + 11.25)\left(\frac{0.4975}{1-0.4975}\right) = 50\ \text{V} \tag{56}$$

$$C_{2,min} = C_{3,min} = I_{o,rated} \times \frac{(1-D_b)T_s}{0.001 \times V_{C2}} = 0.3488 \times \frac{(1-0.4975) \times 10\mu}{0.001 \times 50} = 35.1\ \mu\text{F} \tag{57}$$

Finally, the value of C_2 or C_3 is set at 47 μF.

5.9. Design of C_o

By assuming that the maximum ripple voltage of C_o is 0.1% of V_{Co}, and based on [21], the value of $C_{o,min}$ can be worked out as follows:

$$\begin{aligned} \Delta i_{Lo} &= \tfrac{1}{n}(V_{in2} + V_{C1}) \times D_b \times T_s \div L_o \\ &= \tfrac{1}{0.5} \times (14 + 11.25) \times 0.4975 \times 10\mu \div 4.32\text{m} \\ &= 0.0587\ \text{A} \end{aligned} \tag{58}$$

$$ESR = \frac{0.001 \times V_o}{\Delta i_{Lo}} = \frac{0.001 \times 100}{0.0587} = 1.704\ \Omega \tag{59}$$

$$ESR \times C_{o,min} = 50 \sim 80\mu \Rightarrow C_{o,min} = \frac{80\mu}{1.704} = 46.08\ \mu\text{F} \tag{60}$$

Eventually, the value of C_o is set at 68 μF.

5.10. Converter Topology Comparison

In Table 6, two circuits shown in [19] and [20] are employed as comparisons. The number of components is used as a comparison item, to be described below. From Table 6, it can be seen that the proposed converter has the smallest number of components.

Table 6. Comparison between the existing [19,20] and the proposed circuits.

Component No.	[19]	[20]	Proposed
Input	2	2	2
Inductor	3	3	2
Coupled Inductor	2	1	1
Switch	4	2	2
Diode	4	5	3
Charge Pump Capacitor	4	1	3

6. Simulated and Experimental Results

6.1. Simulated Results

A PSIM-based simulation was utilized to demonstrate the feasibility of this system with the designed resistance of 313 Ω (100 V/348 mA) used as a load. Since in the PSIM software only a solar cell model can be utilized, the parameters of this model were modified to simulate TEG operation. There are three examples to be discussed, as follows:

In example 1, displayed in Figure 17, it can be seen that the generated power relevant to TEG1 is 22.976 W, and this value is close to the MPP power of 23.142 W, while the generated power relevant to TEG2 is 11.029 W, and this value is close to the MPP power of 11.7 W. Summing the two powers yields 34.005 W, and this value is almost the same as the output power of 34.065 W. Moreover, the output voltage is 98.81 V, which is close to 100 V. In addition, the corresponding duty cycles of D_c and D_d are 0.578 and 0.52, respectively, and these values are somewhat different from 0.6 and 0.4975 under voltage mode control, respectively.

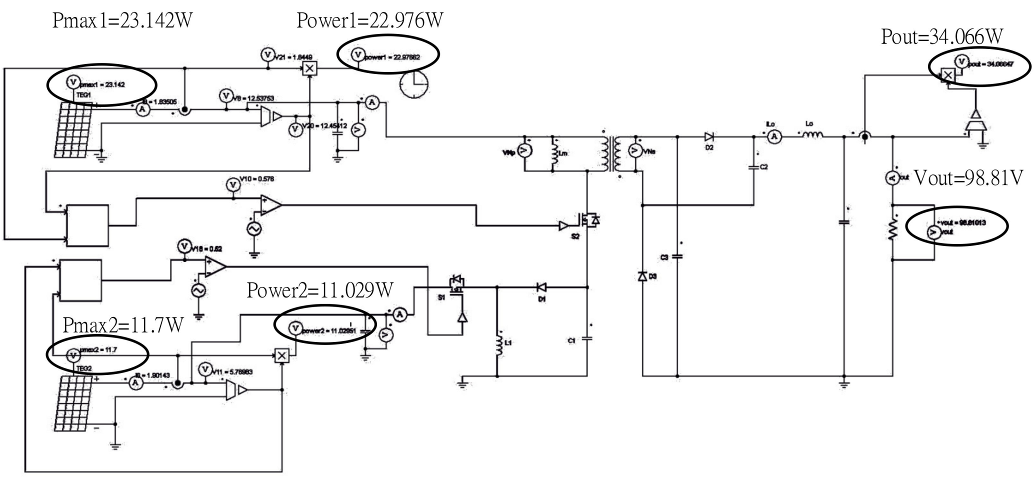

Figure 17. Simulation example 1.

In example 2, displayed in Figure 18, the short current I_{sc} of TEG1 is three times that of TEG1 in Figure 17. From Figure 18, it can be seen that the generated power relevant to TEG1 is 67.004 W, and this value is close to the MPP power of 69.426 W, while the generated power relevant to TEG2 is 10.45 W, and this value is close to the MPP power of 11.7 W. Summing the two powers yields 77.454 W, and this value is close to the output power of 76.835 W. Moreover, the output voltage is 148.39 V, and this is because the more the power is transferred, the higher the output voltage.

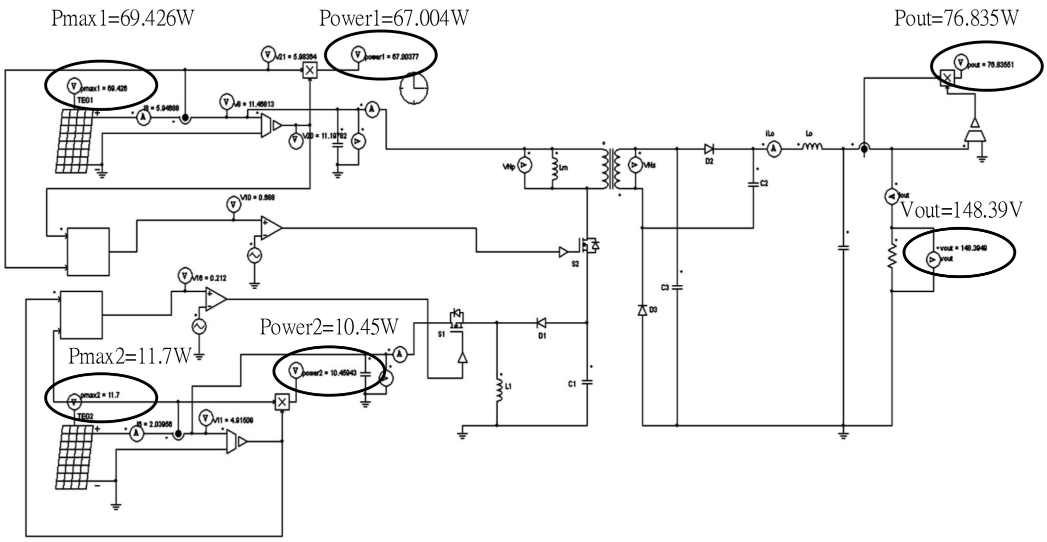

Figure 18. Simulation example 2.

In example 3, displayed in Figure 19, the open voltage V_{oc} of TEG1 is four times that of TEG1 in Figure 17. From Figure 19, it can be seen that the generated power relevant to TEG1 is 85.951 W, and this value is close to the MPP power of 85.956 W, while the generated power relevant to TEG2 is 11.28 W, and this value is close to the MPP power of 11.7 W. Summing the two powers yields 97.231 W, and this value is close to the output power of 93.81 W. Moreover, the output voltage is 163.97 V, and this is because the more the power is transferred, the higher the output voltage.

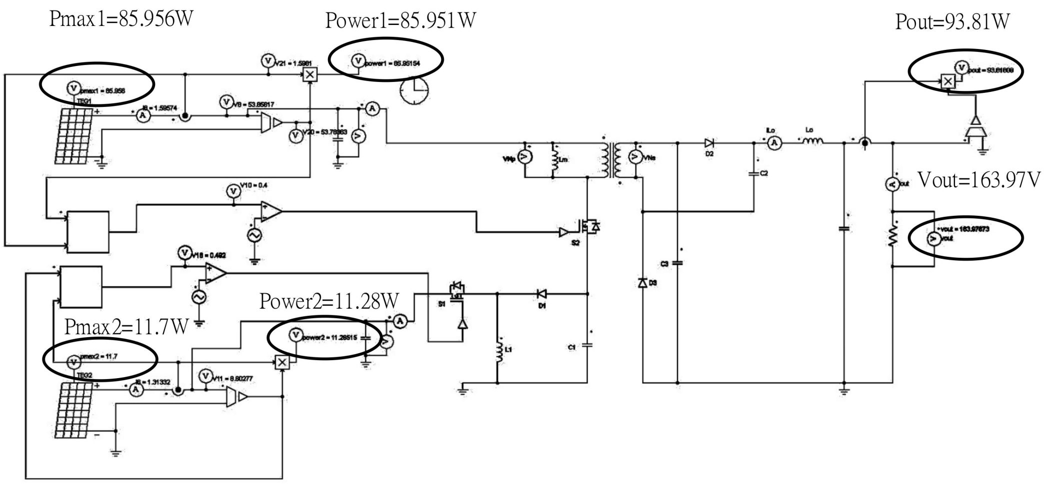

Figure 19. Simulation example 3.

6.2. Efficiency Curve

An efficiency curve can be attained under the output voltage regulated at 100 V, with the electronic load working in the constant current (CC) mode. From Figure 20, it can be seen that the efficiency at 10% load is ~72.2%, the efficiency at 100% load is ~85.2%, and the maximum efficiency is ~87.2%. The reason that the efficiency is not high is the low current in the load.

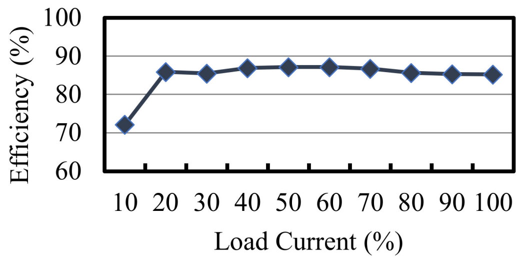

Figure 20. Curve of efficiency versus load current.

6.3. Measured Waveforms

After the efficiency curve is finished, the MPPT algorithm is applied to the proposed converter to demonstrate the maximum power transfer, with some illustrated waveforms given. Note that for MPPT experiments, an electronic load works in the constant voltage (CV) mode.

In the following section, the waveforms shown from Figures 21–26 are measured under MPPT. Figure 21 shows the gate-driving signals v_{gs1} and v_{gs2} for S_1 and S_2, respectively, and the voltages across S_1 and S_2, called v_{ds1} and v_{ds2}, respectively; Figure 22 displays the gate-driving signal v_{gs1} for S_1, the voltage across D_1, the current flowing through L—represented as i_L—and the voltage across C_1; Figure 23 shows the gate-driving signal v_{gs2} for S_2, and the voltages across D_2 and D_3, represented as v_{D2} and v_{D3}, respectively; Figure 24 displays the gate-driving signal v_{gs2} for S_2, the input current i_{in2}, the secondary-side current i_{Ns}, and the output current i_{Lo}; Figure 25 shows the output voltage V_o, and the voltages across C_2 and C_3, represented as V_{C2} and V_{C3}, respectively; Figure 26 displays the output voltage V_o, and the input voltages V_{in1} and V_{in2}, which are created from TEG1 and TEG2, respectively.

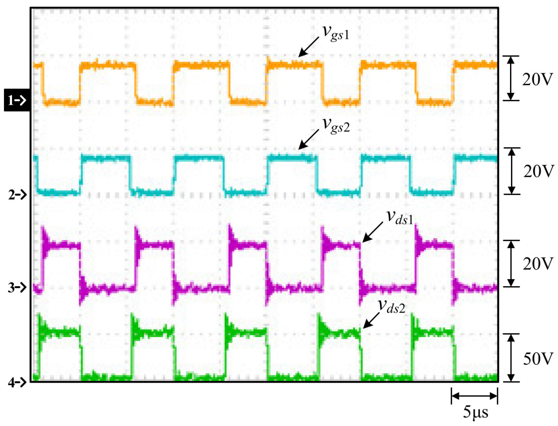

Figure 21. Waveforms measured under the thermoelectric system: (1) v_{gs1}; (2) v_{gs2}; (3) v_{ds1}; (4) v_{ds2}.

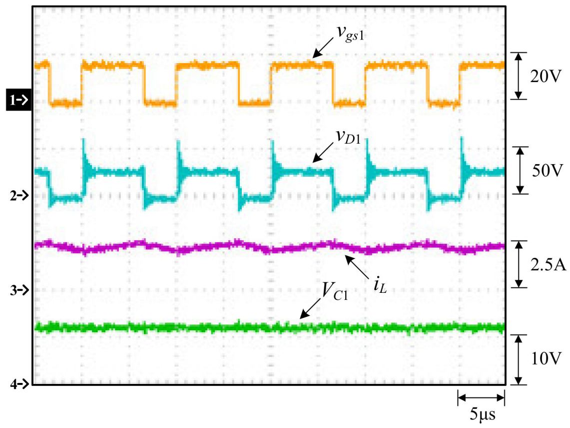

Figure 22. Waveforms measured under the thermoelectric system: (1) v_{gs1}; (2) v_{D1}; (3) i_L; (4) V_{C1}.

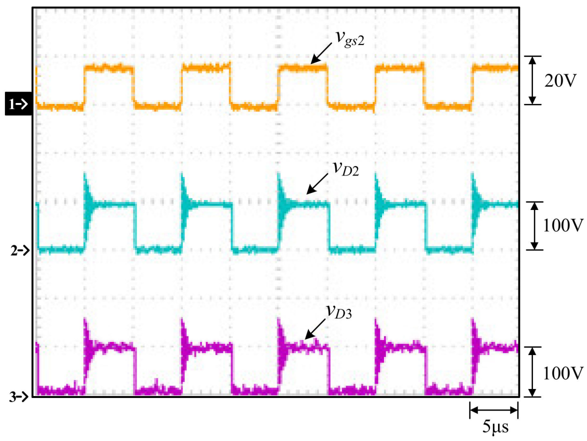

Figure 23. Waveforms measured under the thermoelectric system: (1) v_{gs2}; (2) v_{D2}; (3) v_{D3}.

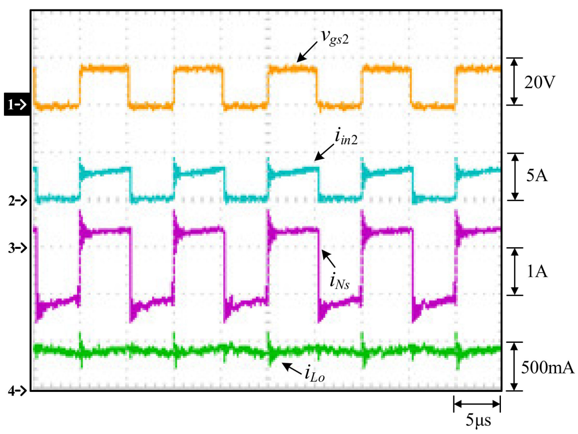

Figure 24. Waveforms measured under the thermoelectric system: (1) v_{gs2}; (2) i_{in2}; (3) i_{Ns}; (4) i_{Lo}.

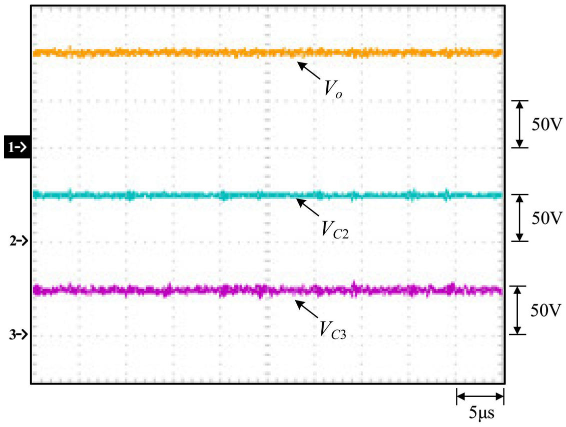

Figure 25. Waveforms measured under the thermoelectric system: (1) V_o; (2) V_{C2}; (3) V_{C3}.

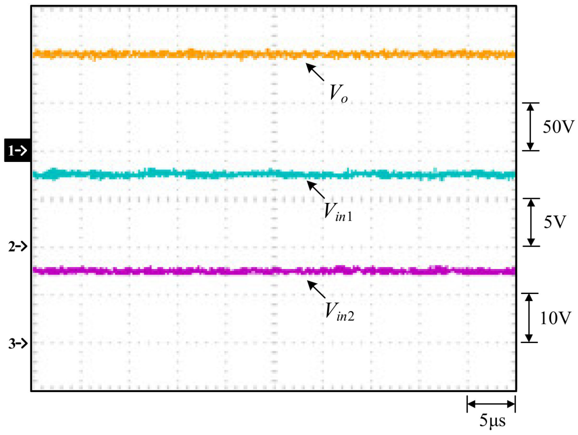

Figure 26. Waveforms measured under the thermoelectric system: (1) V_o; (2) V_{in1}; (3) V_{in2}.

From Figure 21, it can be seen that the maximum voltages across S_1 and S_2 are approximately 20 V and 50 V, respectively. From Figure 22, it can be seen that the maximum voltage across the diode D_1 is ~25 V, with high-frequency oscillation due to the parasitic capacitance of D_1 resonating with the line parasitic inductance, while the voltage across C_1 is ~13 V, and the average value of i_L is ~2.3 A, implying that the average value of i_{in1} is ~1.6 A, and that TEG1 works at MPP. From Figure 23, it can be seen that the maximum voltages across the diodes D_2 and D_3 are ~100 V, with high-frequency oscillation due to the parasitic capacitances of D_2 and D_3 resonating with the line parasitic inductance and the secondary-side leakage inductance L_{lk2}. From Figure 24, it can be seen that the average value of i_{Lo} is 350 mA, and the average value of i_{in2} is ~1.5 A, implying that TEG2 works at MPP. Figure 25 shows that the value of V_o is ~100 V, while the values of V_{C2} and V_{C3} are ~50 V, meaning that the voltages across the two capacitors C_2 and C_3 can be kept constant at the desired value. Figure 26 shows that the value of V_o is ~100 V, the value of V_{in1} is ~7.5 V, and the value of V_{in2} is ~14 V, implying that the two TEGs operate under individual MPPs. Figure 27 shows photos of the proposed thermoelectric system containing the MISOC circuit and the thermoelectric platform.

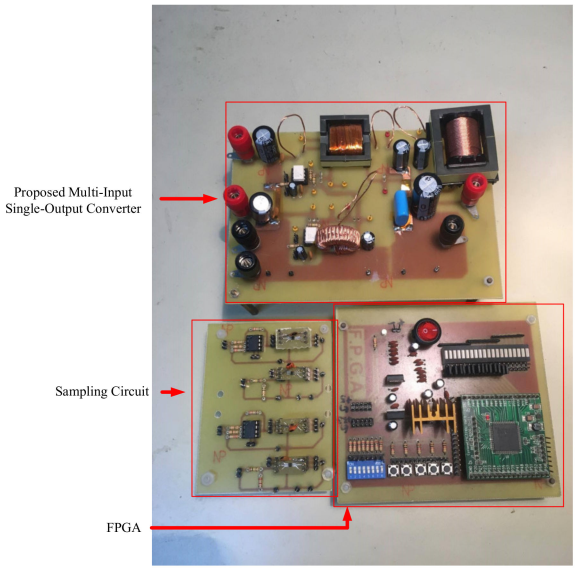

(**a**)

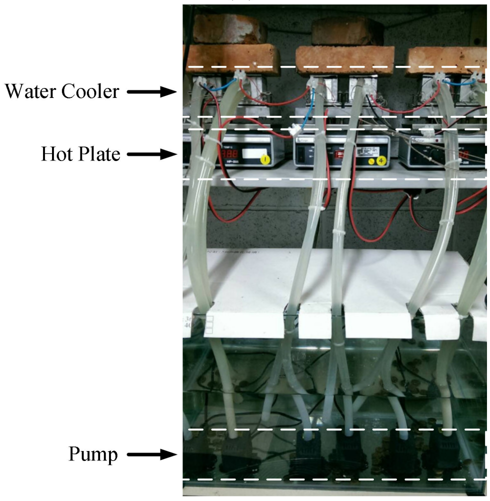

(**b**)

Figure 27. Photos of the proposed thermoelectric system: (**a**) MISOC circuit; (**b**) thermoelectric platform.

7. Conclusions

The presented isolated MISOC circuit was analyzed and imposed on a one-stage thermal energy harvesting system. In this system, TEGs possess individual MPPT functions, thus rendering the thermal energy harvesting more efficient. Moreover, the presented converter has a relatively high step-up ratio. Furthermore, the input count can be increased, indicating that more TEGs can be connected to such a converter with individual MPPT functions. Finally, future works should aim to increase the power level along with the soft switching technology applied.

Author Contributions: Conceptualization, Y.-T.Y. and K.-I.H.; methodology, Y.-T.Y.; software, J.-J.S.; validation, Y.-T.Y., K.-I.H. and J.-J.S.; formal analysis, Y.-T.Y.; investigation, J.-J.S.; resources, Y.-T.Y.; data curation, J.-J.S.; writing—original draft preparation, K.-I.H.; writing—review and editing, K.-I.H.; visualization, J.-J.S.; supervision, K.-I.H.; project administration, K.-I.H.; funding acquisition, J.-J.S. All authors have read and agreed to the published version of the manuscript.

Funding: This research was funded by the Ministry of Science and Technology, Taiwan, under the Grant Number: MOST 110-2221-E-035-050.

Institutional Review Board Statement: Not applicable.

Informed Consent Statement: Not applicable.

Data Availability Statement: No new data were created or analyzed in this study. Data sharing is not applicable to this article.

Conflicts of Interest: The authors declare no conflict of interest.

References

1. Karpe, S. Thermoelectric power generation using waste heat of automobile. *Int. J. Curr. Eng. Technol.* **2016**, *4*, 144–148.
2. Testa, A.; De Caro, S.; Scimone, T.; Cacciato, M.; Scelba, G. A NPC step-up inverter for thermo-electric generators. In Proceedings of the 2015 International Conference on Clean Electrical Power (ICCEP), Taormina, Italy, 16–18 June 2015; pp. 780–785. [CrossRef]
3. John, J.; Jose, J. A new three phase step up multilevel inverter topology for renewable energy applications. In Proceedings of the 2016 International Conference on Circuit, Power and Computing Technologies (ICCPCT), Nagercoil, India, 18–19 March 2016; pp. 1–5. [CrossRef]
4. Sanz, A.; Vidaurrazaga, I.; Pereda, A.; Alonso, R.; Roman, E.; Martinez, V. Centralized vs. distributed (power optimizer) PV system architecture field test results under mismatched operating conditions. In Proceedings of the 2011 37th IEEE Photovoltaic Specialists Conference, Seattle, WA, USA, 19–24 June 2011; pp. 2435–2440. [CrossRef]
5. Liu, Y.-C.; Chen, Y.-M. A systematic approach to synthesizing multi-input DC–DC converters. *IEEE Trans. Power Electron.* **2009**, *24*, 116–127. [CrossRef]
6. Lam, J.; Jain, P.K. A novel electrolytic capacitor-less multi-input DC/DC converter with soft-switching capability for hybrid renewable energy system. In Proceedings of the 2014 16th European Conference on Power Electronics and Applications, Lappeenranta, Finland, 26–28 August 2014; pp. 1–10. [CrossRef]
7. Haghighian, S.K.; Hosseini, S.H. A novel multi-input DC/DC converter with a general power management strategy for grid connected hybrid PV/FC/battery system. In Proceedings of the 6th Power Electronics, Drive Systems and Technologies Conference (PEDSTC2015), Tehran, Iran, 3–4 February 2015; pp. 1–6. [CrossRef]
8. Lara-Salazar, G.; Vázquez, N.; Hernández, C.; López, H.; Arau, J. Multi-input DC/DC converter with battery backup for renewable applications. In Proceedings of the 2016 13th International Conference on Power Electronics (CIEP), Guanajuato, Mexico, 20–23 June 2016; pp. 47–51. [CrossRef]
9. Akar, F. A high-efficiency bidirectional non-isolated multi-input converter. In Proceedings of the 2016 19th International Symposium on Electrical Apparatus and Technologies (SIELA), Bourgas, Bulgaria, 29 May–1 June 2016; pp. 1–4. [CrossRef]
10. Delshad, M.; Harchegani, A.T.; Karimi, M.; Mahdavi, M. A new ZVT multi-input converter for hybrid sources systems. In Proceedings of the 2016 International Conference on Applied Electronics (AE), Pilsen, Czech Republic, 6–7 September 2016; pp. 61–64. [CrossRef]
11. Zhang, N.; Sutanto, D.; Muttaqi, K.M. A buck-boost converter based multi-input DC-DC/AC converter. In Proceedings of the 2016 IEEE International Conference on Power System Technology (POWERCON), Wollongong, NSW, Australia, 28 September–1 October 2016; pp. 1–6. [CrossRef]
12. Poshtkouhi, S.; Trescases, O. Multi-input single-inductor dc-dc converter for MPPT in parallel-connected photovoltaic applications. In Proceedings of the 2011 Twenty-Sixth Annual IEEE Applied Power Electronics Conference and Exposition (APEC), Fort Worth, TX, USA, 6–11 March 2011; pp. 41–47. [CrossRef]
13. Baddipadiga, B.P.; Ferdowsi, M. A high-voltage-gain dc-dc converter based on modified Dickson charge pump voltage multiplier. *IEEE Trans. Power Electron.* **2016**, *32*, 7707–7715. [CrossRef]
14. Jiang, W.; Fahimi, B. Maximum solar power transfer in multi-port power electronic interface. In Proceedings of the 2010 Twenty-Fifth Annual IEEE Applied Power Electronics Conference and Exposition (APEC), Palm Springs, CA, USA, 21–25 February 2010; pp. 68–73. [CrossRef]
15. Hwu, K.I.; Jiang, W.Z. Analysis, design and derivation of a two-phase converter. *IET Power Electron.* **2015**, *8*, 1987–1995. [CrossRef]
16. Hwu, K.-I.; Yau, Y.-T.; Hsieh, M.-L. Thermoelectric energy conversion system with multiple inputs. *IEEE Trans. Power Electron.* **2019**, *35*, 1603–1621. [CrossRef]
17. Khosrogorji, S.; Torkaman, H.; Karimi, F. A short review on multi-input DC/DC converters topologies. In Proceedings of the 6th Power Electronics, Drive Systems and Technologies Conference (PEDSTC2015), Tehran, Iran, 3–4 February 2015; pp. 650–654. [CrossRef]
18. Li, Y.; Ruan, X.; Yang, D.; Liu, F.; Tse, C.K. Synthesis of multiple-input DC/DC converters. *IEEE Trans. Power Electron.* **2010**, *25*, 2372–2385. [CrossRef]
19. Lam, J.; Jain, K. An asymmetrical PWM (APWM) controlled multi-input isolated resonant converter with zero voltage switching (ZVS) for hybrid renewable energy systems. In Proceedings of the 2014 IEEE 36th International Telecommunications Energy Conference (INTELEC), Vancouver, BC, Canada, 28 September–2 October 2014; pp. 1–6. [CrossRef]
20. Zeng, J.; Qiao, W.; Qu, L. An isolated multiport DC-DC converter for simultaneous power management of multiple renewable energy sources. In Proceedings of the 2012 IEEE Energy Conversion Congress and Exposition (ECCE), Raleigh, NC, USA, 15–20 September 2012; pp. 3741–3748. [CrossRef]

21. Nilsson, J.W.; Riedel, S. *Electric Circuits*, 10th ed.; Pearson Education Inc.: London, UK, 2005.
22. Laird, I.; Lu, D.D.-C. High step-up DC/DC topology and MPPT algorithm for use with a thermoelectric generator. *IEEE Trans. Power Electron.* **2012**, *28*, 3147–3157. [CrossRef]